

ELEMENTARY PARTICLES AND FIELDS

Theory

The Trojan Horse Method in Nuclear Astrophysics*

C. Spitaleri^{1),2)**}, A. M. Mukhamedzhanov³⁾, L. D. Blokhintsev⁴⁾,
M. La Cognata^{1),2)}, R. G. Pizzone²⁾, and A. Tumino^{2),5)}

Received December 21, 2010; in final form, May 13, 2011

Abstract—The study of energy production and nucleosynthesis in stars requires an increasingly precise knowledge of the nuclear reaction rates at the energies of interest. To overcome the experimental difficulties arising from the small cross sections at those energies and from the presence of the electron screening, the Trojan Horse Method has been introduced. The method provides a valid alternative path to measure unscreened low-energy cross sections of reactions between charged particles, and to retrieve information on the electron screening potential when ultra-low energy direct measurements are available.

DOI: 10.1134/S1063778811110184

1. INTRODUCTION

To understand the energy production in stars and related nucleosynthesis processes, the knowledge of nuclear reaction cross sections close to the Gamow energy E_G is required [1–4].

In charged-particle-induced reactions, E_G is far below the Coulomb barrier E_C of the interacting nuclei. Therefore, their cross sections $\sigma_b(E)$ drop exponentially with decreasing energy, $\sigma_b(E) \sim \exp(-2\pi\eta)$ where η is the Sommerfeld parameter depending on the atomic numbers Z_1, Z_2 of the colliding nuclei and on their relative velocity v in the entrance channel, $\eta = Z_1 Z_2 e^2 / (\hbar v)$. Thus, direct $\sigma_b(E)$ measurements suffer for a low-energy limit, which usually extends to energies that are typically much larger than E_G . The extrapolation from measurements at higher energies would be the standard way to obtain $\sigma_b(E_G)$. But extrapolation is complicated because of the exponential variation of the cross section. To obtain the value at the Gamow energy, $\sigma_b(E)$ is usually parameterized in terms of the bare nucleus astrophysical factor $S_b(E)$, as given by:

$$\sigma_b(E) = \frac{1}{E} S_b(E) \exp(-2\pi\eta), \quad (1)$$

where $\exp(-2\pi\eta)$ is the Gamow factor. $S_b(E)$ shows a much weaker energy dependence than the cross section $\sigma_b(E)$, thus it is used to extrapolate the cross section from higher energies ($E > 4E_G$) to the Gamow peak. Such an extrapolation into the unknown can lead to considerable uncertainty and important contributions to the excitation functions, like resonance tails of sub-threshold resonances, can be missed [3, 4].

In the available few accurate direct measurements within, or close to, the Gamow peak (e.g., [5]), an unexpected effect showed up, attributed to the presence of atomic electrons [6]. They have been considered as responsible for the increase of the cross section at low energies, the so-called “electron screening effect” [6].

In the extrapolation of the cross section using Eq. (1), it is assumed that the Coulomb potential of the target nucleus and the projectile is that resulting from bare nuclei (this is why an index b is used for both the cross section and the $S(E)$ factor). However, for nuclear reactions studied in the laboratory, the target nuclei and the projectiles are usually in the form of neutral atoms or molecules and ions, respectively. The electron clouds surrounding the interacting nuclei screen the nuclear charges: the projectile effectively sees a reduced Coulomb barrier, both in height and radial extension. This leads, in turn, to a cross section for the screened nuclei $\sigma_s(E)$, higher than the one we would get in the case of bare nuclei, $\sigma_b(E)$, with an exponential increase of $\sigma_s(E)$ (or equivalently of the astrophysical factor $S_s(E)$) with decreasing energy.

To parameterize the cross section rise due to the screening effect, an enhancement factor f_{lab} is usually introduced. This f_{lab} is defined as:

$$f_{lab}(E) = \sigma_s(E) / \sigma_b(E) \sim \exp(\pi\eta U_e / E), \quad (2)$$

*The text was submitted by the authors in English.

¹⁾Dipartimento di Fisica e Astronomia, Università degli Studi di Catania, Italy.

²⁾Laboratori Nazionali del Sud, INFN, Catania, Italy.

³⁾Cyclotron Institute, Texas A & M University, College Station (TX), USA.

⁴⁾Skobeltsyn Institute of Nuclear Physics, Moscow State University, Russia.

⁵⁾Università degli Studi di Enna “Kore”, Enna, Italy.

**E-mail: spitaleri@lns.infn.it

Table 1. Two-body reactions studied via the THM

No.	Indirect reaction	Direct reaction	$E_{\text{lab}}^{\text{inc}}$, MeV	Q_2 , MeV	TH nucleus (x cluster)	Reference
1	$^2\text{H}(^7\text{Li}, \alpha\alpha)n$	$^1\text{H}(^7\text{Li}, \alpha)^4\text{He}$	19–22	15.122	$^2\text{H}(p)$	[13, 20, 22]
2	$^3\text{He}(^7\text{Li}, \alpha\alpha)d$	$^1\text{H}(^7\text{Li}, \alpha)^4\text{He}$	33	11.853	$^3\text{H}(p)$	[23]
3	$^2\text{H}(^6\text{Li}, \alpha^3\text{He})n$	$^1\text{H}(^6\text{Li}, \alpha)^3\text{He}$	22–34	1.795	$^2\text{H}(p)$	[21, 24]
4	$^6\text{Li}(^6\text{Li}, \alpha\alpha)^4\text{He}$	$^2\text{H}(^6\text{Li}, \alpha)^4\text{He}$	5	22.372	$^6\text{Li}(d)$	[25–27]
5	$^2\text{H}(^9\text{Be}, \alpha^6\text{Li})n$	$^1\text{H}(^9\text{Be}, \alpha)^6\text{Li}$	22	−0.099	$^2\text{H}(p)$	[28]
6	$^2\text{H}(^{10}\text{B}, \alpha^7\text{Be})n$	$^1\text{H}(^{10}\text{B}, \alpha)^7\text{Be}$	27	6.3	$^2\text{H}(p)$	[29]
7	$^2\text{H}(^{11}\text{B}, \alpha^8\text{Be})n$	$^1\text{H}(^{11}\text{B}, \alpha)^8\text{Be}$	27	6.3	$^2\text{H}(p)$	[30, 31]
8	$^2\text{H}(^{15}\text{N}, \alpha^{12}\text{C})n$	$^1\text{H}(^{15}\text{N}, \alpha)^{12}\text{C}$	60	2.74	$^2\text{H}(p)$	[32, 33]
9	$^2\text{H}(^{18}\text{O}, \alpha^{15}\text{N})n$	$^1\text{H}(^{18}\text{O}, \alpha)^{15}\text{N}$	54	1.76	$^2\text{H}(p)$	[34, 35]
10	$^2\text{H}(^{17}\text{O}, \alpha^{14}\text{N})n$	$^1\text{H}(^{17}\text{O}, \alpha)^{14}\text{N}$	41	−1.032	$^2\text{H}(p)$	[36]
11	$^6\text{Li}(^3\text{He}, p^4\text{He})^4\text{He}$	$^2\text{H}(^3\text{He}, p)^4\text{He}$	5–6	16.878	$^6\text{Li}(d)$	[37]
12	$^2\text{H}(^6\text{Li}, p^3\text{H})^4\text{He}$	$^2\text{H}(d, p)^3\text{H}$	14	2.59	$^6\text{Li}(d)$	[38]
13	$^6\text{Li}(^{12}\text{C}, \alpha^{12}\text{C})^2\text{H}$	$^4\text{He}(^{12}\text{C}, ^{12}\text{C})^4\text{He}$	20.16	0	$^6\text{Li}(\alpha)$	[39]
14	$^2\text{H}(^6\text{Li}, t^4\text{He})^1\text{H}$	$n(^6\text{Li}, t)^4\text{He}$	14	2.224	$^2\text{H}(n)$	[40, 41]
15	$^2\text{H}(p, pp)n$	$^1\text{H}(p, p)^1\text{H}$	5–6	2.224	$^2\text{H}(p)$	[19]

where U_e is the electron screening potential.

Clearly, a good understanding of U_e is needed in order to calculate σ_b from the experimental σ_s using Eq. (2). In turn, the understanding of U_e , which is different from the screening potential in the stellar plasma U_{pl} , may help to better understand the same U_{pl} , needed to calculate σ_{pl} [6, 7].

Since the astrophysical $S(E)$ factor for bare nuclei at E_G is not available experimentally, extrapolation, usually supported by theoretical arguments, is needed in order to evaluate the bare one. It means that extrapolation is needed even when measured cross sections are available in the Gamow energy range. To overcome the experimental difficulties of direct measurements, several indirect methods such as Coulomb Dissociation [8], Asymptotic Normalization Coefficients [9, 10], and Trojan Horse Method (THM) [11–18] have been developed in the last 20 years. Among them, the THM is at present the only powerful technique to measure $\sigma_b(E)$ of reactions between charged particles at never reached energies (see [13, 19–41] in Table 1). It makes it possible also to retrieve independent information on the electron screening potential when direct ultra-low energy measurements are available.

2. BASIC THEORY

The THM selects the quasi-free (QF) contribution of an appropriate three-body reaction $A + B \rightarrow C + D + S$ [11, 12], performed at energies well above the Coulomb barrier, to extract a charged-particle two-body reaction cross section $B + x \rightarrow C + D$ at astrophysical energies free of Coulomb suppression [19].

It should be stressed that the THM has its scientific background in the theory of direct reaction mechanisms (see, e.g., [42]), and in particular in the studies of the QF reaction mechanisms [12]. The application to nuclear astrophysics is an extension to the low energies of the well assessed higher-energy measurements of the QF three-body reactions [20, 21, 43].

In the present paper, the THM is presented within the Plane Wave Impulse Approximation (PWIA) framework and applied to nonresonant reactions with dominant $l = 0$ partial wave contribution. The motivations for such a simplified approach in the application of the THM are discussed. In particular, some of the basic critical points of this simplified approximation are presented. More sophisticated theoretical formulations can be found in [11, 15, 16, 18, 25]. The QF $B(A, CD)S$ reaction between B and

the projectile A , whose wave function is assumed to have a large amplitude for the $A = xS$ cluster configuration, can be described by a Feynman diagram (Fig. 1), where only the first term of the Feynman series is retained [44–46]. The diagram represents the dominant process (pole approximation), while other graphs (triangle graphs) indicating rescattering between the reaction products, are neglected [45]. Under these hypotheses, the particle B is considered to interact only with a part (x cluster) of the nucleus A , while the other part (S cluster) is considered as spectator to the $B(x, C)D$ virtual reaction.

In the impulse approximation (IA) the three-body reaction cross section is proportional to the cross section of the binary reaction [47]. Following the simple PWIA, the three-body reaction can be factorized into two terms corresponding to the vertices of Fig. 1 and it is given by [48, 49]:

$$\frac{d^3\sigma}{d\Omega_C d\Omega_D dE_C} \propto (\text{KF}) |\phi(p_S)|^2 \left[\frac{d\sigma(E)}{d\Omega} \right]^{\text{HOES}}. \quad (3)$$

Here:

(1) $\left[\frac{d\sigma(E)}{d\Omega} \right]^{\text{HOES}}$ is the half-off-energy-shell (HOES) differential cross section for the binary $B(x, C)D$ reaction at the center-of-mass energy E given in post-collision prescription (PCP) by the relation [50]

$$E = E_{CD} - Q_{2b}, \quad (4)$$

where Q_{2b} is the Q value for the binary $x + B \rightarrow C + D$ reaction and E_{CD} is the CD relative energy in the exit channel;

(2) KF is a kinematical factor containing the final-state phase-space factor and is a function of the masses, momenta, and angles of the outgoing particles [51]

$$\text{KF} = \frac{(m_B + m_x)(m_C + m_D)k_C k_D}{\hbar^2 m_x k_A} \frac{K_i}{K_f} \times \left[1 + \frac{m_C}{m_S} + \frac{m_C}{m_S} \frac{k_C}{k_D} \cos \theta_{CD} - \frac{m_D}{m_B} \frac{k_B}{k_D} \cos \theta_D \right]^{-1},$$

where K_i and K_f are the relative wave numbers in the initial and final states, θ_{CD} is the relative angle between the directions of detection of particles C and D ;

(3) $\phi(p_S)$ is the Fourier transform of the radial wave function for the $\chi(\mathbf{r}_{xS})$ intercluster motion usually described in terms of Hankel, Eckart, or Hulthén functions depending on the xS system.

In the applications of the THM the two-cluster xS system in the nucleus A is most likely in s state, thus the expected momentum distribution has a maximum at $p_S = 0$.

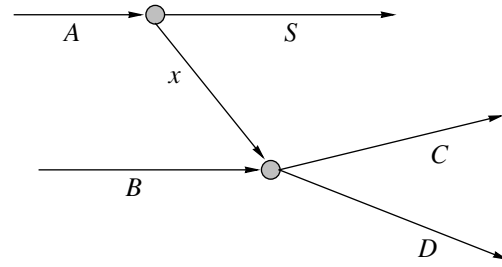


Fig. 1. Feynman diagram representing the quasi-free $A(B, CD)S$ reaction.

In Table 2 some examples of QF reactions already investigated are given.

To completely determine the kinematical properties of the S particle, in particular its momentum distribution, energies E_C and E_D and emission angles θ_C and θ_D of the two particles C and D must be measured.

The resulting two-dimensional energy spectrum ($E_C - E_D$) obtained from such a measurement is usually reduced to a one-dimensional spectrum by projecting the coincidence yield onto one of the energy axes (E_C or E_D) (see [13, 30]).

2.1. Energy and Momentum Prescriptions

Beam energies have been carefully chosen to optimize the kinematical conditions for the presence of QF mechanism under the assumptions of the IA.

The study of QF processes was previously done in high Q -value three-body reactions induced on light nuclei at low energy. QF effects are usually expected in reactions where high momenta (≥ 300 MeV/c) are involved, even at low energy due to high Q values. The beam energy is chosen in such a way as to overcome the Coulomb barrier $(E_{AB})^{\text{CB}}$ in the entry channel (Table 2). Thus, particle x is brought inside the nuclear interaction zone to induce the relevant reaction $x + B \rightarrow C + D$. The QF kinematical conditions must be chosen in such a way that relative energy E_{xB} can span the astrophysical region of interest below the Coulomb barrier $(E_{xB})^{\text{CB}}$ [11].

This is possible because the initial projectile velocity is compensated for by the binding energy of particle x inside A ([13, 30] and references therein). Thus, the xB relative energy of the fragments can be very low. In symbols, we have:

$$E = E_{xB} - B_{xS} = E_{\text{QF}}, \quad (5)$$

with E_{xB} being the projectile energy in the two-body center-of-mass system and B_{xS} the xS binding energy. It is very important to experimentally validate the correctness of the pole approximation in each

Table 2. Three-body QF reactions studied: Energies, momentum transfer q_t , and associated wave length λ

No.	Indirect reaction	E_{xS}^{CB} , MeV	E_{AB}^{CB} , MeV	E_{lab}^{inc} , MeV	E_{cm}^{inc} , MeV	Q_{val}^{2-body} , MeV	E_{cm}^{tot} , MeV	q_t , MeV/c	λ , Fm	Reference
1	${}^2\text{H}({}^7\text{Li}, \alpha\alpha)n$	1.14	1.06	19–22	4.22	15.22	19.342	391	3.16	[13, 20, 22]
2	${}^3\text{He}({}^7\text{Li}, \alpha\alpha)d$	1.14	1.98	33	23	11.85	34.96	236	6.1	[23]
3	${}^2\text{H}({}^6\text{Li}, \alpha{}^3\text{He})n$	1.18	1.08	14.25	3.5	1.795	5.295	263	4.7	[21, 24]
4	${}^6\text{Li}({}^6\text{Li}, \alpha\alpha){}^4\text{He}$	1.08	2.74	5	2.5	22.372	24.872	250	5.12	[26]
5	${}^2\text{H}({}^9\text{Be}, \alpha{}^6\text{Li})n$	1.44	1.33	22	4.0	−0.099	3.901	360	3.9	[28]
6	${}^2\text{H}({}^{11}\text{B}, \alpha{}^8\text{Be})n$	1.72	1.59	27	4.15	6.36	10.51	370	3.8	[30, 31]
7	${}^2\text{H}({}^{15}\text{N}, \alpha{}^{12}\text{C})n$	2.23	2.08	60	7.05	2.74	9.79	645	1.97	[32, 33]
8	${}^2\text{H}({}^{18}\text{O}, \alpha{}^{15}\text{N})n$	2.45	2.28	54	5.4	1.76	7.16	668	1.8	[34, 35]
9	${}^2\text{H}({}^{17}\text{O}, \alpha{}^{14}\text{N})n$	2.48	2.31	41	4.31	−1.032	3.278	560	2.75	[36]
10	${}^6\text{Li}({}^3\text{He}, p{}^4\text{He}){}^4\text{He}$	0.41	1.02	5.6	4.67	16.878	21.558	460	2.69	[37]
11	${}^2\text{H}({}^6\text{Li}, p{}^3\text{H}){}^4\text{He}$	0.44	1.08	14	3.5	2.59	6.09	186	3.13	[38]
12	${}^6\text{Li}({}^{12}\text{C}, \alpha{}^{12}\text{C}){}^2\text{H}$	3.42	4.85	20.16	6.67	0	6.67	262	2	[39]
13	${}^2\text{H}({}^6\text{Li}, t{}^4\text{He}){}^1\text{H}$	1.18	1.08	14	3.5	2.224	5.724	190	8.1	[40]
14	${}^2\text{H}(p, pp)n$	0.55	0.49	5.6	3.33	2.224	5.554	75	16.4	[19]

specific case [46]. The applicability of the pole approximation is limited to small p_{xS} with a prescription given by [46]:

$$0 \leq p_S \leq k_{xS} \quad (6)$$

with p_S being the HOES momentum of the cluster x when it interacts with the particle B , and k_{xS} defined by the relation $k_{xS} = \sqrt{2\mu_{xS}B_{xS}}$ where μ_{xS} is the reduced mass.

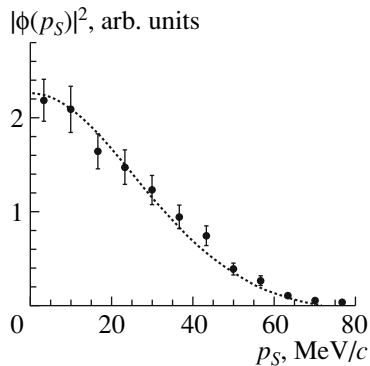


Fig. 2. Deuteron experimental momentum distribution (full dots) extracted from ${}^2\text{H}({}^{11}\text{B}, \alpha{}^8\text{Be})n$ reaction compared with the theoretical one (dotted curve).

2.2. Experimental Momentum Distribution in Impulse Approximation

The presence of the QF mechanism can be checked by means of a shape analysis of the measured xS momentum distribution $|\phi(p_S)|^2$. If the cross section is known, $|\phi(p_S)|^2$ can be obtained from the QF yield with the energy-sharing method or by measuring an angular correlation.

The momentum distribution $|\phi(p_S)|^2$ is obtained, in the energy-sharing approach, by selecting a narrow relative energy windows ΔE and center-of-mass angular range $\Delta\theta_{cm}$.

This is done by considering the relative energy spectrum E_{CD} vs. p_S . The procedure is shown in Fig. 2 for the ${}^2\text{H}({}^{11}\text{B}, \alpha{}^8\text{Be})n$ reaction [30]. If the factorization of Eq. (3) is applicable, dividing the quasifree coincidence yield (Y) by the kinematic factor, a quantity which is proportional to the product of the momentum distribution by the $x + B \rightarrow C + D$ two-body cross section is obtained. In a restricted relative energy ΔE and center-of-mass angular range, the differential binary cross section can be considered almost constant and

$$|\phi(p_S)_{\text{exp}}|^2 \propto \frac{Y}{KF}. \quad (7)$$

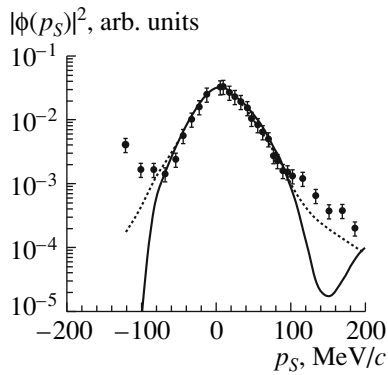


Fig. 3. ${}^6\text{Li}$ momentum distribution obtained through the ${}^6\text{Li}(p, p\alpha){}^2\text{H}$ reaction (full dots). The normalization is done equalizing the maximum value of the theoretical distributions to the maximum value of the experimental data. The full (dashed) curve is the DWIA (PWIA) distribution [52].

In Fig. 2 the experimental momentum distribution for the proton inside the deuteron for the ${}^2\text{H}({}^{11}\text{B}, \alpha{}^8\text{Be})n$ reaction at $E_{11\text{B}} = 27$ MeV is reported. The squared Hulthén function (dotted curve) in momentum space is superimposed onto the data. The theoretical momentum distribution extracted from Eq. (7) reproduces quite well the shape of experimental data. The theoretical $\text{FWHM} = 58$ MeV/c is in good agreement with the experimental one [30].

The momentum distributions calculated in the PWIA and DWIA (Distorted Wave Impulse Approximation) might differ both in their absolute value and their shape [52–54]. However, at high incident energies (more than about 100 MeV for $(p, p\alpha)$ (see Fig. 3), (p, pd) , and $(\alpha, 2\alpha)$ reactions) the two calculations have essentially the same shape at least for values of the spectator cluster momenta smaller than about 60 MeV/c. At lower energies, absorption and distortion effects become more important, so that the validity of the PWIA is less and less justified [55]. The usual treatment in the PWIA yields, in fact, narrower momentum distributions with a FWHM between 40 and 60 MeV/c, so that in the standard procedure to fit data, a cutoff distance in the radial part $R_R(r)$ of the inter-cluster wave function $\chi(\mathbf{r})$ is introduced. Many experiments [43, 51, 56, 57] to study QF processes in high- Q -value three-body reactions induced on light nuclei at low incident energy were performed. Besides the PWIA approach, the DWIA treatment was sometimes applied in the analysis of QF reactions and QF scatterings. In the DWIA [52, 58], the radial wave functions are deduced from optical-model potentials and the following considerations apply:

(i) at low relative momenta, the shapes of the DWIA and PWIA distributions coincide. However,

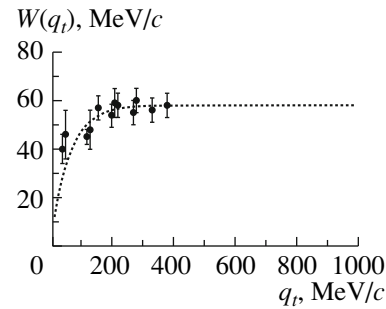


Fig. 4. Width [FWHM] for the momentum distribution of the proton inside the deuteron as a function of the transferred momentum q_t (full dots). The curve superimposed onto the data represents an empirical fit described in [60] and references therein.

while PWIA introduces unphysical zeros in the momentum distribution, the DWIA represents a more realistic approach;

(ii) in DWIA treatment the absolute value of the momentum distribution undergoes a dramatic decrease due to the wave absorption effects, which are not taken into account in PWIA.

An important point to be stressed is that in the THM only events with a spectator momentum close to the QF condition (cutoff of few tens of MeV/c) are taken into account. In the case:

(i) the essential features of the $|\phi(p_S)|^2$ are the same in both procedures within the experimental uncertainties;

(ii) the differences in the absolute values can be recovered from the normalization to the experimental data.

In the case of nonresonant reactions at low incident energies but with high Q value, the standard procedure is totally reliable. Conversely, in reactions with both low incident energies and Q values distortions might intervene introducing more marked differences between the PWIA and DWIA momentum distributions. These distortions are responsible for a drastic change of the width (FWHM) in the spectator momentum distribution [57, 59, 60].

The curve in Fig. 4 shows the trend of the momentum distribution widths from experimental data available in the literature as a function of transferred momentum q_t from A to the system $B = C + D$; it is determined as the Galilean-invariant transferred momentum [60]. In Table 2, a number of experimental cases is shown. In particular, in the case of the ${}^{11}\text{B} + d$ reaction at incident energy of 27 MeV and transferred momentum of 370 MeV/c, the value of the experimental FWHM is 58 MeV/c. Thus, it matches its asymptotic value of 58 MeV/c (Fig. 4). In some experimental works it was necessary to reduce the

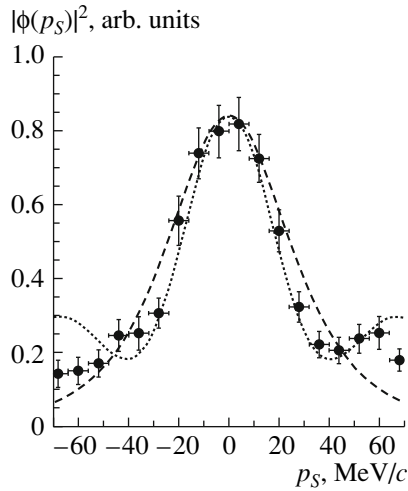


Fig. 5. Experimental pn momentum distribution (full dots) from $^{18}\text{O}(d, \alpha^{15}\text{N})n$ reaction compared with the theoretical ones, given by the square of the Hulthén function in PWIA (dashed curve) and by the DWBA momentum distribution evaluated using FRESKO code (dotted curve) [35].

theoretical FWHM in order to reproduce the experimental distribution.

Besides supplying a more realistic description of the experimental momentum distributions, the DWIA approach is necessary to extract spectroscopic information from the experimental data. In DWIA the radial wave functions are deduced from optical-model potentials so that in Eq. (3), they turn out to be dependent on the considered reaction as well as on the energy [52, 54]:

$$\frac{d^3\sigma}{d\Omega_C d\Omega_D dE_C} \quad (8)$$

$$= (\text{KF})(S_{LJ})(\Sigma_\lambda |T^{L\lambda}|^2) \left[\frac{d\sigma}{d\Omega} \right]^{\text{OES}}$$

with KF the kinematic factor of Eq. (3), S_{LJ} the cluster spectroscopic factor, $\Sigma |T^{L\lambda}|^2$ often referred to as distorted momentum distribution (see [58, 52]).

In the limit of no distortions the above expressions reduce to the PWIA: the distorted waves reduce to plane waves and the quantity $\Sigma |T^{L\lambda}|^2$ is proportional to the Fourier transform of the xS bound-state wave function.

As already mentioned, in the analysis of THM applications the PWIA is usually adopted since it fairly describes the experimental data. Anyway, to check the validity of the PWIA approach and to reproduce those data where distortions cannot be neglected, the more realistic Distorted Wave Born Approximation (DWBA) should be employed. The experimental data [34–36, 61] show that even in the DWBA if we

limit our event selection to the region close to the maximum of the momentum distribution, DWBA and PWIA approaches give the same results. We will consider data of the $^{18}\text{O}(p, \alpha)^{15}\text{N}$ -reaction studied using a deuteron as the “Trojan Horse” nucleus [35].

The pn PWIA momentum distribution from $^{18}\text{O}(p, \alpha)^{15}\text{N}$ QF reaction is shown in Fig. 5 as a dashed curve. The dashed curve reproduces the experimental behavior for $p_S \leq 50$ MeV/c, while for larger momenta it departs from the experimental data. The normalization factor is obtained by scaling the calculated distribution to the experimental one (see [35]). The DWBA calculations is instead given by a dotted curve in the same figure. It has been performed by means of the FRESKO computer code, taking the optical-model potential parameters from C.M. Perey and F.C. Perey [62]. In the range 0 to 50 MeV/c, the difference between PWIA and DWBA momentum distributions is negligibly small, about 4%, in comparison with other uncertainties. Same considerations apply to the $^{17}\text{O}(p, \alpha)^{14}\text{N}$ reaction [36]. These results strengthen the importance and reliability of the PWIA approach.

3. DATA ANALYSIS

In general, relatively simple experimental setups in the THM experiments are needed. The main requirements are high energy and angular resolutions. Usually the detection setup consists of two or more couples of coincidence telescopes arranged at opposite side of the beam direction at quite forward angles, the experiments being usually performed in inverse kinematics. Kinematical calculations, in general, show the strong dependence of the E_{xB} uncertainty on the angular resolution of both ejectiles. That is why in our experiments an angular resolution of the order of 0.1° – 0.5° is required.

A number of steps are involved in the data analysis before the two-body cross section of astrophysical relevance can be extracted. These steps include:

- (1) selection of the “Trojan Horse” nucleus;
- (2) identification of events due to the three-body reaction of interest $A + B \rightarrow C + D + S$;
- (3) selection of the QF reaction mechanism;
- (4) extraction of the HOES two-body cross section from the measured three-body one in arbitrary units;
- (5) correction for the penetration probability of the HOES cross section below the Coulomb barrier B_{xB} ;
- (6) normalization procedure to obtain the bare nucleus cross section $\sigma_b(E)$ in absolute units;
- (7) validity tests on the selected events;
- (8) extraction of the electron screening potential when ultra-low energy measurements are available.

3.1. Selection of the “Trojan Horse” Nucleus

A number of indirect investigations with the THM have been focused on the study of (p, α) reactions which play a key role in many stellar nucleosynthesis paths. These measurements are usually performed in inverse kinematics with a “deuteron target” as a “virtual-proton” target. The choice of a deuteron as the “Trojan Horse” (TH) nucleus is suggested by a number of reasons:

- (i) its binding energy is low;
- (ii) its wave function is well known;
- (iii) it has a unique simple cluster structure (proton plus neutron);
- (iv) the cluster spectator is not charged;
- (v) the inter-cluster xS motion takes place at $l = 0$, thus the momentum distribution has a maximum for $p_S = 0$.

In Table 3 a list of possible TH nuclei is reported with the corresponding virtual x participant. It is clear that different choices of TH nuclei are available to get the same virtual x .

We note from Table 3 that, for example, a virtual participant proton can be hidden either inside a deuteron ${}^2\text{H} = (p + n)$ with $n = \text{spectator}$ (binding energy $B_{pn} = 2.225$ MeV) or inside ${}^3\text{He} = (p + d)$ with $d = \text{spectator}$ ($B_{pd} = 5.49$ MeV).

The choice of best particle A (TH nucleus) in the $A + B \rightarrow C + D + S$ three-body reaction to study the $x + B \rightarrow C + D$ two-body reaction is mainly linked to:

- (i) the binding energy of the xS cluster system in the TH nucleus;
- (ii) the appropriate incident energy of the projectile;
- (iii) the Q -value of $A + B \rightarrow C + D + S$ three-body reaction;
- (iv) the energy range of the excitation function for the two-body relevant reaction to be investigated;
- (v) the different contributing reaction mechanisms with the three particles C , D , and S in the final state (Sequential Decay and Direct Breakup).

Another very important point to emphasize is that all TH nuclei (${}^2\text{H}$, ${}^6\text{Li}$, ${}^3\text{He}$, ${}^{16}\text{O}$) used so far in the performed experiments (Table 4) are always characterized by an $l = 0$ orbital angular momentum for the inter-cluster xS motion. In this condition, the momentum distribution shows a peak at $p_S = 0$. This choice is linked not only to the reduction of experimental difficulties when selecting the QF mechanism but also to theoretical considerations for the applicability of the pole approximation [46]. Indeed, the extension to measurements with TH nuclei having

Table 3. Main features of the candidates as “Trojan Horse” nuclei

No.	TH nucleus	$x-S$	l	Binding energy, MeV
1	${}^2\text{H}$	$p-n$	0	2.22
2	${}^3\text{H}$	$d-n$	0	6.26
3	${}^3\text{He}$	$p-d$	0	5.49
4	${}^6\text{Li}$	$d-\alpha$	0	1.47
5	${}^7\text{Li}$	$t-\alpha$	1	2.47
6	${}^7\text{Be}$	${}^3\text{He}-\alpha$	1	1.58
7	${}^{16}\text{O}$	$\alpha-{}^{12}\text{C}$	0	7.16

$l = 1$ is desirable as it would allow for the investigation of nuclear reactions induced by virtual ${}^3\text{H}$ and ${}^3\text{He}$, obtained from the cluster systems ${}^7\text{Li} = t-\alpha$ and ${}^7\text{Be} = \alpha-{}^3\text{He}$, respectively (see Table 4).

3.2. QF Data Selection: Study of the Momentum Distribution in Angular Correlation

A way to discriminate between sequential decay (SD) and QF events is through an angular correlation analysis of the data. Coincidence data are projected onto the C (or D) energy axis E_C (or E_D) at a fixed angle for one of the two particles and different angles for the other particle. Figure 6 shows examples of the angular correlation analysis for the ${}^2\text{H}({}^3\text{H}, dd)n$ reaction at a beam energy of 35.5 MeV for a deuteron angle $\theta_{d1} = 20^\circ$ and angles for the other deuteron $\theta_{d2} = 20^\circ$ to 40° . Since the momentum distribution of the pn system in ${}^2\text{H}$ has a maximum for $(p_S)^{\min} = 0$, the feature expected for a QF reaction is a coincidence yield attaining a maximum when $(p_S)^{\min}$ approaches zero [63, 64]. The $(\theta_{d1}, \theta_{d2})$ angles corresponding to this condition represent the so-called QF angles. In the spectra of Fig. 6, three typical features appear:

- (i) a broad peak around $(p_S)^{\min}$ is observed (marked with an arrow);
- (ii) this peak does not correspond to excited states of the ${}^4\text{He}$ or ${}^3\text{H}$ intermediate systems (see [63] for details);
- (iii) the yield of the broad peak is larger at $(p_S)^{\min} = 0$, and decreases while moving away from zero.

This represents the first necessary check for the existence of the QF mechanism. In general, the presence of SD contribution can make this test much more complicate.

Table 4. k_S limit of pole approximation applicability and the selected Δp_S ranges in the QF experiments

No.	Indirect reaction	E_{AB} , MeV	k_S , MeV/c	Δp_S , MeV/c	Reference
1	${}^2\text{H}({}^7\text{Li}, \alpha\alpha)n$	20	45	0–40	[13, 20, 22]
2	${}^3\text{He}({}^7\text{Li}, \alpha\alpha)d$	33	83	0–30	[23]
3	${}^2\text{H}({}^6\text{Li}, \alpha{}^3\text{He})n$	14, 25	45	0–30	[21, 24]
4	${}^6\text{Li}({}^6\text{Li}, \alpha\alpha){}^4\text{He}$	5	61	0–35	[26]
5	${}^2\text{H}({}^9\text{Be}, \alpha{}^6\text{Li})n$	22	45	0–20	[28]
6	${}^2\text{H}({}^{11}\text{B}, \alpha{}^8\text{Be})n$	27	45	0–40	[30, 31]
7	${}^2\text{H}({}^{15}\text{N}, \alpha{}^{12}\text{C})n$	60	45	0–40	[32, 33]
8	${}^2\text{H}({}^{18}\text{O}, \alpha{}^{15}\text{N})n$	54	45	0–40	[34, 35]
9	${}^2\text{H}({}^{17}\text{O}, \alpha{}^{14}\text{N})n$	41	83	0–30	[36]
10	${}^6\text{Li}({}^3\text{He}, p{}^4\text{He}){}^4\text{He}$	5–6	61	0–20	[37]
11	${}^2\text{H}({}^6\text{Li}, p{}^3\text{H}){}^4\text{He}$	14	61	0–10	[38]
12	${}^6\text{Li}({}^{12}\text{C}, \alpha{}^{12}\text{C}){}^2\text{H}$	20.16	61	0–10	[39]
13	${}^2\text{H}({}^6\text{Li}, t{}^4\text{He}){}^1\text{H}$	14	45	0–20	[40]
14	${}^2\text{H}(p, pp)n$	5–6	45	0–20	[19]

3.3. QF Data Selection: Study of the Relative Energy E_{cm} as Function of Δp_S

Another way to test the presence of QF and/or SD mechanism is to investigate the correlation between the coincidence yield in a selected relative energy window, and the momentum p_S for all coincident events. This test can be repeated for different relative energy intervals spanning the energy region of interest, and if the agreement with the theoretical momentum distribution is always confirmed, one can be sure about the correct selection of the QF mechanism. Figure 7 shows the experimental yield distribution (full dots), integrated over $E = 150 \pm 50$ keV and $\Delta\theta_{cm} = 90^\circ - 110^\circ$, as a function of undetected particle momentum p_S projected in the p_S range: $0 < p_S < 20$ MeV/c, $20 < p_S < 40$ MeV/c, and $55 < p_S < 75$ MeV/c, compared with the Hulthén theoretical distribution (solid curve). The good agreement makes us confident on the validity of the procedure to select the QF mechanism.

3.4. Extraction of the Two-Body Cross Section from the Measured Three-Body Reaction

If the experimental momentum distribution $|\phi(p_S)^{\text{exp}}|^2$ is known, one can extract the HOES

cross section from the three-body coincidence yield:

$$\left[\frac{d\sigma}{d\Omega}\right]^{\text{HOES}} \propto \left[\frac{Yd}{(\text{KF})|\phi(p)^{\text{exp}}|^2}\right]. \quad (9)$$

In the analysis, the product $(\text{KF})|\phi(p_S)^{\text{exp}}|^2$ is usually provided by means of a Monte-Carlo calculation. We stress that this relation is valid as far as the pole approximation is applicable. To get the absolute value, the cross section can be normalized to the binary reaction in an energy range ΔE above the Coulomb barrier.

In the THM applications, the reaction $x + B \rightarrow C + D$ is induced inside the short-range of the B nuclear field. Thus, the HOES cross section represents the nuclear part only. For this reason, the penetration probability of the Coulomb barrier has to be introduced to compare the THM cross section with the direct data from literature in the energy region below the Coulomb barrier.

4. VALIDITY TESTS OF THE POLE APPROXIMATION

Equation (3), for the pole graph represented in Fig. 1, has the remarkable characteristic that the reaction amplitude is factorized, i.e., it can be written as the product of two amplitudes and a propagator,

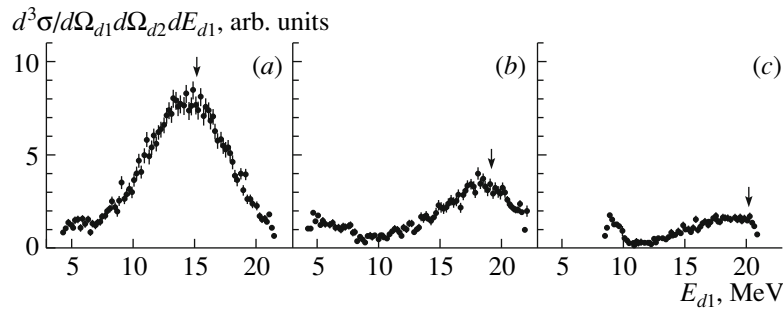


Fig. 6. Typical angular correlation spectra for the $^2\text{H}(^3\text{H}, dd)n$ reaction at beam energy of 35.5 MeV: (a) $p_S = 6.60$ MeV/c, $\theta_{d2} = 20^\circ$; (b) $p_S = 30.2$ MeV/c, $\theta_{d2} = 30^\circ$; (c) $p_S = 66.5$ MeV/c, $\theta_{d2} = 40^\circ$. Coincidence data are projected onto the E_{d1} variable for $\theta_{d1} = 20^\circ$ [63]. The meaning of broad peaks marked with an arrow is explained in the text.

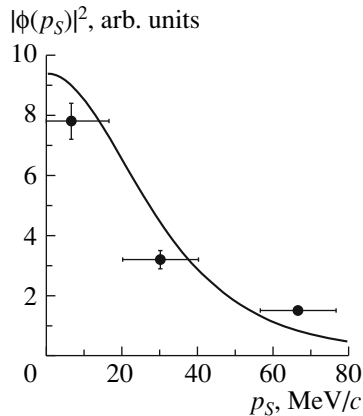


Fig. 7. $^2\text{H}(^3\text{H}, dd)n$ reaction. Experimental yield distribution (full dots) compared with the theoretical momentum distribution given in terms of a Hulthén function (solid curve) [63].

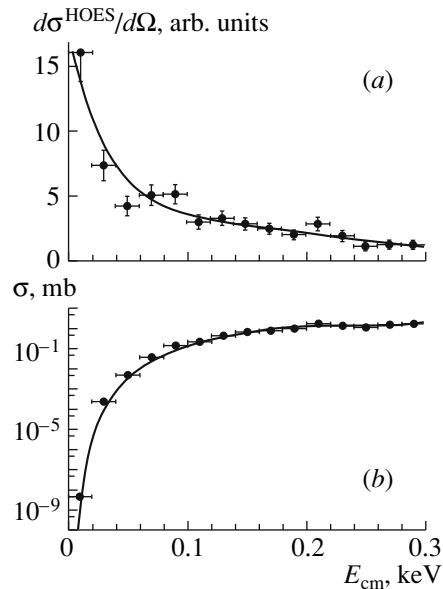


Fig. 8. (a) Example of nuclear two-body differential cross section from a TH experiment; (b) TH two-body cross section already multiplied by the P_l as explained in the text.

and depends only on three variables instead of five as in the general case. These characteristics make it possible to express the differential cross section of the reaction through that of the virtual process in the right-hand vertex (the $x + B \rightarrow C + D$ reaction). In the PWIA as well as in the DWIA the three-body reaction cross section is proportional to the cross section of the virtual two-body reaction (Eq. (3)). Thus, the factorization test can be used. Different tests of the pole approximation mechanism have been proposed at low energies. As already mentioned, the analysis of the experimental results for three-body reactions is complicated by the presence of other reaction mechanisms, constituting a background for QF data. Because of the uncertainties that can be introduced by the presence of this background in the applicability of the IA, a series of experiments were carried out to provide some critical tests of pole approximation or of the IA. We present hereafter some tests allowing us to validate the pole approximation. They apply to the behavior of the indirect excitation

function: both excitation function $\sigma(E)$ and angular distributions $\sigma(\theta_{\text{cm}})$ of the binary reaction $x + B \rightarrow C + D$ must be compared with the corresponding two-body $\sigma(E)^{\text{HOES}}$ excitation function and angular distributions $\sigma(\theta_{\text{cm}})^{\text{HOES}}$, respectively (see [30] and references therein).

4.1. Comparison of Excitation Functions

4.1.1. $\sigma(E)$ above the Coulomb Barrier. If the energy E_{xB} of the xB relative motion is higher than the Coulomb barrier E^{CB} between the particles in the entrance channel of the $x + B \rightarrow C + D$ reaction, a necessary condition for the pole approximation is:

$$\sigma(E_{\text{cm}})^{\text{HOES}} \propto \sigma(E_{\text{cm}})^{\text{OES}}. \quad (10)$$

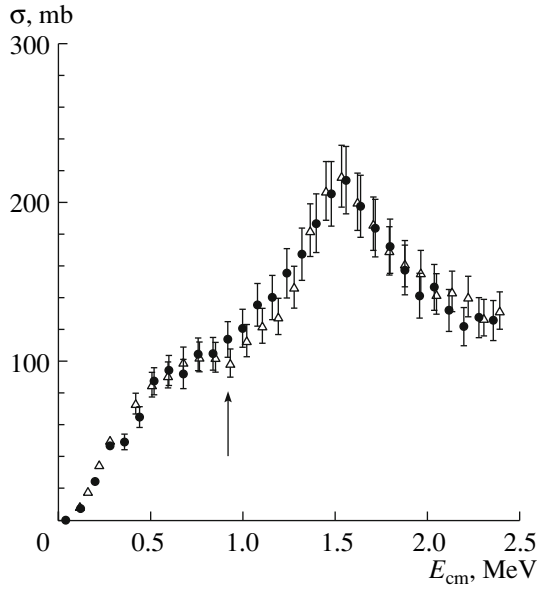


Fig. 9. Cross section of the QF ${}^6\text{Li}(p, \alpha){}^3\text{He}$ reaction (full dots) extracted from the ${}^2\text{H}({}^6\text{Li}, \alpha{}^3\text{He})n$ QF reaction [24]. Direct data [24] are reported as open triangles. An arrow marks the Coulomb barrier.

4.1.2. Below the Coulomb Barrier. If E_{xB} is smaller than the Coulomb barrier E^{CB} , to compare the results with those from direct measurements it is necessary to correct the HOES cross section for the penetration function P_l through the Coulomb barrier (see Fig. 8); a necessary condition for the validity of the pole approximation is that the cross section of the two-body reaction $\sigma(E_{cm})^{TH}$ is proportional to the binary direct reaction $\sigma(E_{cm})^{OES}$:

$$\sigma(E_{cm})^{TH} = \sigma(E_{cm})^{HOES} P_l(k_{xB}r_{xB}) \quad (11)$$

$$\propto \sigma(E_{cm})^{OES},$$

where the penetration probability of the Coulomb barrier is defined by the equation:

$$P_l(k_{xB}r_{xB}) = \frac{k_{xB}r_{xB}}{F_l^2(k_{xB}r_{xB}) + G_l^2(k_{xB}r_{xB})} \quad (12)$$

with F_l and G_l being the regular and irregular Coulomb wave functions, k_{xB} and r_{xB} being the xB relative wave number and interaction radius, respectively.

4.1.3. Above and below the Coulomb Barrier. In some cases, it is possible to accomplish for both above conditions at the same time. For details see [24, 23]. Figure 9 shows the behavior of the excitation function for the ${}^6\text{Li}(p, \alpha){}^3\text{He}$ reaction extracted from the QF contribution to the ${}^2\text{H}({}^6\text{Li}, \alpha{}^3\text{He})n$ experiment [24]. Experimental TH data are shown as full dots, while open triangles are direct data as given in [24]. Another example of the TH ${}^7\text{Li}(p, \alpha){}^4\text{He}$

cross section is reported in Fig. 10. This experiment was performed using ${}^3\text{He}$ as TH nucleus. The solid curve represents the free two-body-reaction cross section integrated over the whole solid angle. The very good agreement in both cases validates the pole approximation and supports the basic idea that the result, at least for the ${}^7\text{Li} + p$ reaction, is not TH nucleus dependent.

4.2. Comparison of the Angular Distributions: Above and Below the Coulomb Barrier

As a second test a comparison between the indirectly extracted angular distributions and the direct behavior is performed. The relevant angle to get the indirect angular distributions can be calculated according to [65] for the spectator in the target,

$$\theta_{cm} = \arccos \frac{(\mathbf{v}_B - \mathbf{v}_x) \cdot (\mathbf{v}_C - \mathbf{v}_D)}{|\mathbf{v}_B - \mathbf{v}_x| |\mathbf{v}_C - \mathbf{v}_D|} \quad (13)$$

and for the spectator in the projectile by

$$\theta_{cm} = \arccos \frac{(\mathbf{p}_S) \cdot (\mathbf{v}_C - \mathbf{v}_D)}{|\mathbf{p}_S| |\mathbf{v}_C - \mathbf{v}_D|}. \quad (14)$$

A necessary condition for the pole approximation is that the total cross section of the two-body $\sigma(\theta_{cm})^{HOES}$ reaction is proportional to the binary direct reaction $\sigma(\theta_{cm})^{OES}$:

$$\sigma(\theta_{cm})^{HOES} \propto \sigma(\theta_{cm})^{OES}. \quad (15)$$

This applies both above and below E^{CB} . Indeed, the effect of $P_l(k_{xB}r_{xB})$ on the angular distributions, which is calculated for a given E_{cm} , is only the introduction of an overall scaling factor. Typical results referring to the indirect study of the ${}^{11}\text{B}(p, \alpha){}^8\text{Be}$ reaction are reported in Fig. 11.

5. RESULTS

The THM provides an independent bare nucleus cross-section measurement, $\sigma_b(E)$ (or equivalently the bare nucleus astrophysical factor $S_b(E)$). Thus, it is possible to extract information on the electron screening potential [22] by comparing $S_b(E)$ with the one obtained from shielded nuclei. Once the two-body cross section has been extracted, the THM astrophysical $S(E)$ factor can be obtained according to:

$$[S_b(E)]^{THM} = E \cdot [\sigma_b(E)]^{THM} \exp(-2\pi\eta). \quad (16)$$

Thus, the energy dependence of $[S_b(E)]^{THM}$ should show the same trend of that derived by the direct measurements $[S_b(E)]$, except in the ultra-low energy

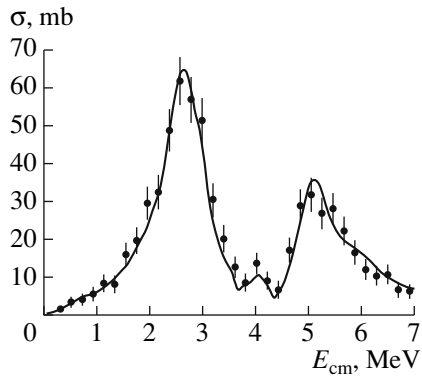


Fig. 10. Cross section of the ${}^7\text{Li}(p, \alpha){}^4\text{He}$ reaction extracted from the ${}^7\text{Li}({}^3\text{He}, \alpha\alpha){}^2\text{H}$ QF reaction [23]. The solid curve represents the free two-body reaction cross section averaged over the angle and energy spread in the experiment. Full dots correspond to the present work.

range ΔE_{ES} where the two data sets should differ due to the effects of electron screening:

$$[S_b(E)]^{\text{THM}} \propto [S_b(E)], \quad (17)$$

where $E > \Delta E_{\text{ES}}$. If needed, the value for the electron screening potential U_e can then be obtained by comparing the two data sets. As already mentioned, the THM does not allow us to extract the absolute value of the astrophysical S factor. However, the absolute scale for $[S_b(\Delta E)]^{\text{THM}}$ can be obtained by normalization of the THM data to the direct ones at energies E^* , where the electron screening effects are negligible

$$N_{\text{abs.value}} = \frac{[S_b(E^*)]^{\text{OES}}}{[S_b(E^*)]^{\text{THM}}}. \quad (18)$$

In case of resonances, the normalization is performed equalizing the areas of the same resonance in both THM and direct data.

6. ASTROPHYSICS APPLICATIONS: THE LIGHT ELEMENT DEPLETION PROBLEM

The abundances of light elements, such as lithium, beryllium, and boron, play a key role in a number of astrophysical problems yet to be completely solved, such as the Big Bang nucleosynthesis and the light nuclei depletion. Both production and destruction mechanisms must be studied and their cross sections should be measured at the energies of astrophysical interest. The (p, α) reactions are crucial for the light element destruction in stellar environment ($E_{\text{cm}} = 1\text{--}50$ keV) and the cross sections (or reaction rates) of these reactions are necessary inputs for the astrophysical models of light element abundances in the universe. In this context, great efforts have

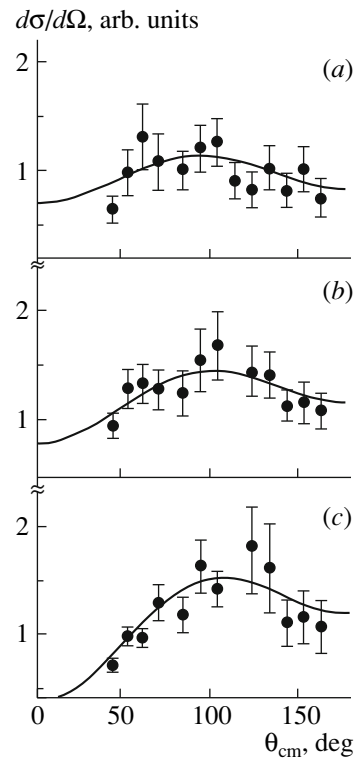


Fig. 11. Experimental angular distributions (full dots) and their analytical approximations (solid curves) showing the ${}^{11}\text{B} + p$ differential cross section as a function of θ_{cm} : (a) $E_{\text{cm}} = 500$ keV; (b) $E_{\text{cm}} = 700$ keV; (c) $E_{\text{cm}} = 900$ keV. The ${}^{11}\text{B} + p$ relative energy range is covered in steps of $\Delta E_{\text{cm}} = 200$ keV [30].

been devoted to the study, both directly and via THM, of relevant reactions, such as ${}^7\text{Li}(p, \alpha){}^4\text{He}$ [13, 22, 66], ${}^6\text{Li}(p, \alpha){}^3\text{He}$ [24], ${}^6\text{Li}(d, \alpha){}^4\text{He}$ [25–27], ${}^9\text{Be}(p, \alpha){}^6\text{Li}$ [28], ${}^{10}\text{B}(p, \alpha){}^7\text{Be}$ [29], ${}^{11}\text{B}(p, \alpha){}^8\text{Be}$ [30] at astrophysical energies.

For some of them, in particular for those involving the lithium isotopes, it has also been possible to extract the electron screening potentials $[U_e]^{\text{THM}}$, which were found to be in agreement with the direct $[U_e]^{\text{dir}}$ estimates, but with much smaller errors. In the following sections we will describe the results in detail.

6.1. The ${}^7\text{Li}(p, \alpha){}^4\text{He}$ Reaction

The cross section $\sigma(E)$ of the ${}^7\text{Li}(p, \alpha){}^4\text{He}$ reaction has been measured in a wide energy range, $E_{\text{cm}} = 15$ keV to $E_{\text{cm}} > 10$ MeV (see [67] and references therein). The directly measured $S(E)$ factor is enhanced at sub-Coulomb energies ($E_{\text{cm}} \leq 100$ keV) because of the electron screening. An extrapolation procedure based on a polynomial expansion was used

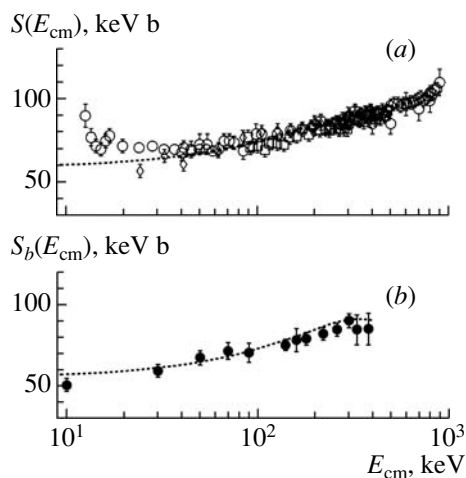


Fig. 12. (a) Direct data (open circles) on $S_b(E)$ for the ${}^7\text{Li}(p, \alpha){}^4\text{He}$ from [68]; the dotted curve is the extrapolation from higher energies using a second-order polynomial fit; (b) THM $S_b(E)$ factor for the ${}^7\text{Li}(p, \alpha){}^4\text{He}$ (full dots) [22]; the dotted curve is the result of the R -matrix calculation reported in [22].

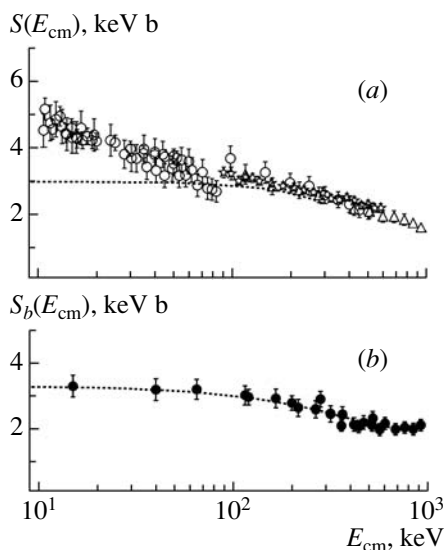


Fig. 13. Astrophysical $S(E)$ factor for the ${}^6\text{Li}(p, \alpha){}^3\text{He}$ reaction: (a) direct data (open circles) from [73–75]; the dotted curve is extrapolated from higher-energy data using a second-order polynomial function; (b) THM $S_b(E)$ factor for the ${}^6\text{Li}(p, \alpha){}^3\text{He}$; the dotted curve is the result of the second-order polynomial fit to THM data.

to obtain information on $S_b(0)$. Both direct data and extrapolation (dotted curve) are reported in Fig. 12a.

To bypass these extrapolations, $S_b(E)$ was extracted applying the THM to the ${}^2\text{H}({}^7\text{Li}, \alpha\alpha)n$ three-body reaction. The ${}^7\text{Li}$ beam incident energy was 19–21 MeV. In the data analysis the simpler PWIA formalism was used. Data [22] were also analyzed

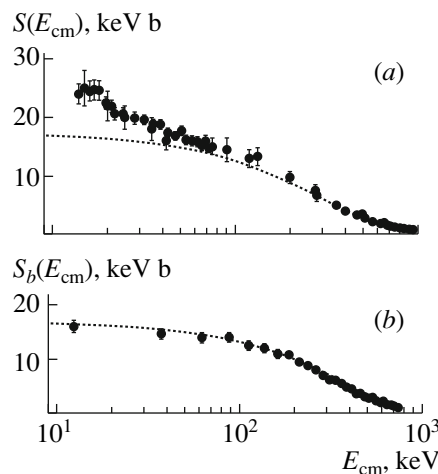


Fig. 14. Astrophysical $S(E)$ factor for the ${}^6\text{Li}(d, \alpha){}^4\text{He}$ reaction: (a) direct data (full dots) from [68] and extrapolated $S_b(E)$ (dotted curve); (b) THM $S_b(E)$ for the ${}^6\text{Li}(d, \alpha){}^4\text{He}$ reaction; the dotted curve is the result of a second-order polynomial fit to THM data.

by using the improved Modified Plane Wave Born Approximation (MPWBA) [15] method. The extracted $S_b(E)$ is reported in Fig. 12b [22] together with a new parameterization based on R -matrix calculations [22]. The $S(0)$ parameter was quoted as 55 ± 3 keV b in agreement with the astrophysical factor from direct data [68, 69], and with the value suggested by R -matrix fit [70]. The NACRE compilation [71] and the recent analysis in [72], give a value of 58 keV b, slightly higher than the one obtained via THM. The electron screening potential U_e turns out to be $U_e = 330 \pm 40$ eV [22], in agreement with the determination of $U_e = 300 \pm 160$ eV (molecular) from extrapolation [68]; this has to be compared with the adiabatic limit $(U_e)^{\text{adiab}} = 186$ eV.

6.2. The ${}^6\text{Li}(p, \alpha){}^3\text{He}$ Reaction

As in the previous case, the ${}^6\text{Li}(p, \alpha){}^3\text{He}$ reaction cross section is enhanced at sub-Coulomb energies ($E_{\text{cm}} < 100$ keV) by the electron clouds surrounding the interacting nuclides [6, 7]. An extrapolation procedure is necessary to obtain information at the Gamow energy. Direct data are reported in Fig. 13a, with the polynomial expansion to perform the extrapolation. The THM was thus applied to determine $S_b(E)$ [24].

The cross section of $d({}^6\text{Li}, {}^3\text{He})n$ three-body reaction was measured at 25 MeV of E_{Li} beam energy. The experiment clearly revealed the presence of the QF mechanism proceeding through a virtual two-body reaction between the incident ${}^6\text{Li}$ and the proton in ${}^2\text{H}$.

The QF two-body cross section was compared with the direct data showing a quite good overall agreement in the E_{cm} (${}^6\text{Li}-p$ relative energy) range 0.12–2.4 MeV, with a distinct contribution from the resonant behavior associated with the 7.2 MeV ($5/2^-$) state of ${}^7\text{Be}$ [24]. A further study of the three-body reaction was performed at 14 MeV of beam energy in order to populate the very low-energy part of the ${}^6\text{Li}-p$ bare nucleus $S(E)$ -factor spectrum, down to the Gamow peak [24]. The bare nucleus $S(E)$ factor was extracted in the energy range $E_{\text{cm}} = 0.01$ to 1.2 MeV, and normalized to direct data taken from [73] in the energy range $E_{\text{cm}} = 0.8$ to 1.2 MeV. The normalized low-energy THM data are reported in Fig. 13*b*. The dotted curve in Fig. 13*b* represents the result of a second-order polynomial fit to the THM data providing the $S(0)$ value of $[S_b(0)]^{\text{THM}} = 3.0 \pm 0.19$ MeV b. The zero-energy astrophysical factor extracted via THM $[S_b(0)]^{\text{THM}}$ is consistent with the value extrapolated from direct measurements [68, 71, 73–75], $S_b(0) = 2.86 \pm 0.80$ MeV b. These results lead to unchanged astrophysical implications [76].

According to the direct estimate ($U_e = 440 \pm 80$ eV), the electron screening potential $[U_e]^{\text{THM}} = 435 \pm 40$ eV is not in agreement with the adiabatic limit, which yields $U_e = 186$ eV as in the previous case.

6.3. The ${}^6\text{Li}(d, \alpha){}^4\text{He}$ Reaction

In the same context, the ${}^6\text{Li}(d, \alpha){}^4\text{He}$ -reaction cross section has been measured via the THM applied to the ${}^6\text{Li}({}^6\text{Li}, \alpha\alpha){}^4\text{He}$ three-body reaction. After the standard THM analysis, $S_b(E)$ was extracted in the energy range $E_{\text{cm}} = 10$ –700 keV and normalized to direct data taken from [68] (see Fig. 14*a*) in the energy range $E_{\text{cm}} = 600$ to 700 keV. The normalized THM data are reported in Fig. 14*b*. The dotted curve in the same figure represents the theoretical calculation reported in [23]. The measurement at astrophysical energies was then repeated by means of the THM as it is extensively reported in [26]. The indirect measurement yields $S_b(0)^{\text{THM}} = 16.9 \pm 0.5$ keV b. The result is consistent with the direct estimate of $S_b(E) = 17.4$ keV b [68]. The electron screening potential turns out to be $U_e = 320 \pm 50$ eV, in agreement with the direct determinations of $U_e = 380 \pm 250$ eV and $U_e = 330 \pm 120$ eV [68] but far from the adiabatic limit, as in the previous cases.

The systematic discrepancy between experimental data and adiabatic approximation is evident in all the cases discussed above. This discrepancy has been attributed to the different chemical structure of the target [77]. However, additional experimental and

theoretical investigations are needed to better understand this problem. In any case, the isotopic independence of the electron screening effect, which was already investigated in other works [68], is confirmed.

Inserting the new THM data in the astrophysical codes, no relevant change in reaction rate as well as in the subsequent stellar evolution and primordial nucleosynthesis is found [67, 76]. The lithium depletion problem is therefore not linked to a wrong evaluation of the ${}^6,7\text{Li}(p, \alpha){}^3,4\text{He}$ and ${}^6\text{Li}(d, \alpha){}^4\text{He}$ cross sections but it has its origins in an unsatisfactory evaluation of stellar processes, e.g., convection and/or other nonstandard mixing mechanisms.

7. CONCLUSIONS

The THM has proven to be a powerful method to investigate astrophysical relevant reactions without Coulomb suppression or electron screening effects. This method provides the only existing way to measure the relevant bare nucleus $S(0)$ parameter avoiding the extrapolation. Among future developments, applications of the THM to neutron-induced reactions are planned. As mentioned, a deuteron beam will be used as a virtual source of a neutron beam. Another novel field of application of the THM is that of astrophysical reactions involving radioactive nuclei. The first test on the ${}^{18}\text{F}(p, \alpha){}^{15}\text{O}$ reaction using ${}^2\text{H}$ as TH nucleus has been already performed. Further possible investigations are being planned.

ACKNOWLEDGMENTS

This work was supported in part by the US Department of Energy under grants nos. DE-FG02-93ER40773, DEFG52-06NA26207, by NSF grant no. PHY-0852653, and by the RFBR grant no. 10-02-00096.

REFERENCES

1. E. M. Burbidge, G. R. Burbidge, W. A. Fowler, and F. Hoyle, *Rev. Mod. Phys.* **29**, 547 (1957).
2. W. A. Fowler, *Rev. Mod. Phys.* **56**, 149 (1984).
3. C. Rolfs and W. S. Rodney, *Cauldrons in the Cosmos* (Univ. of Chicago Press, Chicago, 1988).
4. C. Rolfs, *Prog. Part. Nucl. Phys.* **46**, 23 (2001).
5. R. Bonetti et al., *Phys. Rev. Lett.* **82**, 5205 (1999).
6. H. J. Assenbaum, K. Langanke, and C. Rolfs, *Z. Phys. A* **327**, 461 (1987).
7. F. Strieder, C. Rolfs, C. Spitaleri, and P. Corvisiero, *Naturwissenschaften* **88**, 461 (2001).
8. G. Baur, C. A. Bertulani, and H. Rebel, *Nucl. Phys. A* **458**, 188 (1986).

9. A. M. Mukhamedzhanov et al., Phys. Rev. C **56**, 1302 (1997).
10. A. M. Mukhamedzhanov and R. E. Tribble, Phys. Rev. C **59**, 3418 (1999).
11. G. Baur, Phys. Lett. B **178**, 135 (1986).
12. C. Spitaleri, in *Proceedings of the Conference on Problems of Fundamental Modern Physics, II*, Ed. by R. Cherubini, P. Dalpiaz, and B. Minetti (World Sci., 1991), p. 21.
13. C. Spitaleri, M. Aliotta, S. Cherubini, et al., Phys. Rev. C **60**, 055802 (1999).
14. C. Spitaleri, S. Cherubini, A. Del Zoppo, et al., Nucl. Phys. A **719**, C99 (2003).
15. S. Typel and H. Wolter, Few-Body Syst. **29**, 75 (2000).
16. S. Typel and G. Baur, Ann. Phys. (N.Y.) **305**, 228 (2003).
17. A. M. Mukhamedzhanov et al., Eur. Phys. J. A **27**, Suppl. 1, 205 (2006).
18. A. M. Mukhamedzhanov, L. D. Blokhintsev, B. F. Irgaziev, et al., J. Phys. G **35**, 014016 (2008).
19. A. Tumino, C. Spitaleri, A. M. Mukhamedzhanov, et al., Phys. Rev. Lett. **98**, 252502 (2007).
20. M. Zadro, D. Miljanić, C. Spitaleri, et al., Phys. Rev. C **40**, 181 (1989).
21. G. Calvi, M. Lattuada, D. Miljanić, et al., Phys. Rev. C **41**, 1848 (1990).
22. M. Lattuada, R. G. Pizzone, S. Typel, et al., Astrophys. J. **562**, 1076 (2001).
23. A. Tumino, C. Spitaleri, M. L. Sergi, et al., Eur. Phys. J. A **27** (Suppl. 1), 243 (2006).
24. A. Tumino, C. Spitaleri, A. Di Pietro, et al., Phys. Rev. C **67**, 065803 (2003).
25. S. Cherubini, V. N. Kondratyev, M. Lattuada, C. Spitaleri, et al., Astrophys. J. **457**, 855 (1996).
26. C. Spitaleri, S. Typel, R. G. Pizzone, et al., Phys. Rev. C **63**, 055801 (2001).
27. A. Musumarra, R. G. Pizzone, S. Blagus, et al., Phys. Rev. C **64**, 068801 (2001).
28. Q.-G. Wen, C.-B. Li, S.-H. Zhou, et al., Phys. Rev. C **78**, 035805 (2008).
29. S. Romano, L. Lamia, C. Spitaleri, et al., Eur. Phys. J. A **27** (Suppl. 1), 221 (2006).
30. C. Spitaleri, L. Lamia, A. Tumino, et al., Phys. Rev. C **69**, 055806 (2004).
31. L. Lamia, C. Spitaleri, N. Carlin, et al., Nuovo Cimento C **31**, 423 (2008).
32. M. La Cognata, S. Romano, C. Spitaleri, et al., Phys. Rev. C **76**, 065804 (2007).
33. M. La Cognata, V. Z. Goldberg, A. M. Mukhamedzhanov, C. Spitaleri, and R. E. Tribble, Phys. Rev. C **80**, 012801(R) (2009).
34. M. La Cognata, C. Spitaleri, A. M. Mukhamedzhanov, et al., Astrophys. J. **708**, 796 (2010).
35. M. La Cognata, C. Spitaleri, A. M. Mukhamedzhanov, et al., Phys. Rev. Lett. **101**, 152501 (2008).
36. M. L. Sergi, C. Spitaleri, M. La Cognata, et al., Phys. Rev. C **82**, 032801(R) (2010).
37. M. La Cognata, C. Spitaleri, A. Tumino, et al., Phys. Rev. C **72**, 065802 (2005).
38. A. Rinollo, S. Romano, C. Spitaleri, et al., Nucl. Phys. A **758**, 146c (2005).
39. C. Spitaleri, M. Aliotta, P. Figuera, et al., Eur. Phys. J. A **7**, 181 (2000).
40. A. Tumino, C. Spitaleri, C. Bonomo, et al., Eur. Phys. J. A **25** (Suppl. 1), 649 (2005).
41. M. Gulino, C. Spitaleri, S. Cherubini, et al., J. Phys. G **37**, 125105 (2010).
42. G. R. Satchler, *Direct Nuclear Reactions*, International Series of Monographs on Physics (Oxford Univ. Press, 1983).
43. M. Lattuada, F. Riggi, C. Spitaleri, et al., Nucl. Phys. A **458**, 493 (1986).
44. I. S. Shapiro, V. M. Kolybasov, and G. R. Augst, Nucl. Phys. **61**, 353 (1965).
45. I. S. Shapiro, *Interaction of High-Energy Particles with Nuclei*, in *Proceedings of the International School of Physics "Enrico Fermi"*, Course 38, Ed. by T. E. O. Ericson (Academic Press, New York, 1967), p. 210.
46. I. S. Shapiro, Sov. Phys. Usp. **10**, 515 (1968).
47. G. F. Chew and G. C. Wick, Phys. Rev. **85**, 636 (1952).
48. V. G. Neudatchin and Yu. F. Smirnov, At. Energy Rev. **3**, 157 (1965).
49. G. Jacob and Th. A. J. Maris, Rev. Mod. Phys. **38**, 121 (1966).
50. J. Y. Grossiord et al., Phys. Rev. Lett. **32**, 173 (1974).
51. P. G. Fallica, F. Riggi, C. Spitaleri, and C. M. Sutura, Lett. Nuovo Cimento **22**, 547 (1978).
52. P. G. Roos, N. S. Chant, A. A. Cowley, et al., Phys. Rev. C **15**, 69 (1977).
53. M. Jain, P. G. Roos, H. G. Pugh, and H. D. Holmgren, Nucl. Phys. A **153**, 49 (1970).
54. P. G. Roos, L. Rees, and N. S. Chant, Phys. Rev. C **24**, 2647 (1981).
55. S. Barbarino, M. Lattuada, F. Riggi, C. Spitaleri, et al., Nuovo Cimento A **53**, 327 (1979).
56. J. Kasagi, T. Nakagawa, N. Sekine, et al., Nucl. Phys. A **239**, 233 (1975).
57. S. Barbarino, M. Lattuada, F. Riggi, C. Spitaleri, and D. Vinciguerra, Phys. Rev. C **21**, 1104 (1980).
58. N. S. Chant and P. G. Roos, Phys. Rev. C **15**, 57 (1977).
59. R. G. Pizzone, C. Spitaleri, S. Cherubini, et al., Phys. Rev. C **71**, 058801 (2005).
60. R. G. Pizzone, C. Spitaleri, A. Mukhamedzhanov, et al., Phys. Rev. C **80**, 025807 (2009).

61. M. La Cognata, C. Spitaleri, A. M. Mukhamedzhanov, et al., *Astrophys. J.* **708**, 796 (2010).
62. C. M. Perey and F. G. Perey, *At. Data Nucl. Data Tables* **17**, 1 (1976).
63. M. La Cognata, C. Spitaleri, S. Cherubini, et al., *Few-Body Syst.* **44**, 353 (2008).
64. S. Blagus et al., *Z. Phys. A* **337**, 297 (1990).
65. I. Slaus et al., *Phys. Rev. C* **8**, 444 (1973).
66. M. Aliotta, C. Spitaleri, M. Lattuada, et al., *Eur. Phys. J. A* **9**, 435 (2000).
67. R. G. Pizzone, C. Spitaleri, M. Lattuada, et al., *Astron. Astrophys.* **398**, 423 (2003).
68. S. Engstler, G. Raimann, C. Angulo, et al., *Z. Phys. A* **342**, 471 (1992).
69. C. Rolfs and R. W. Kavanagh, *Nucl. Phys. A* **455**, 179 (1986).
70. F. C. Barker, *Phys. Rev. C* **62**, 044607 (2000).
71. C. Angulo et al., *Nucl. Phys. A* **656**, 3 (1999).
72. R. H. Cyburt, *Phys. Rev. D* **70**, 023505 (2004).
73. A. J. Elwyn, R. E. Holland, C. N. Davids, et al., *Phys. Rev. C* **20**, 1984 (1979).
74. W. Gemeinhardt, D. Kamke, and C. Von Rhöneck, *Z. Phys.* **197**, 58 (1966).
75. H. Spinka, T. Tombrello, and H. Winkler, *Nucl. Phys. A* **164**, 1 (1971).
76. R. G. Pizzone, A. Tumino, S. Degl'Innocenti, C. Spitaleri, et al., *Astron. Astrophys.* **438**, 779 (2005).
77. J. Cruz et al., *J. Phys. G* **35**, 014004 (2008).